Electron Paramagnetic Resonance Spectroscopy

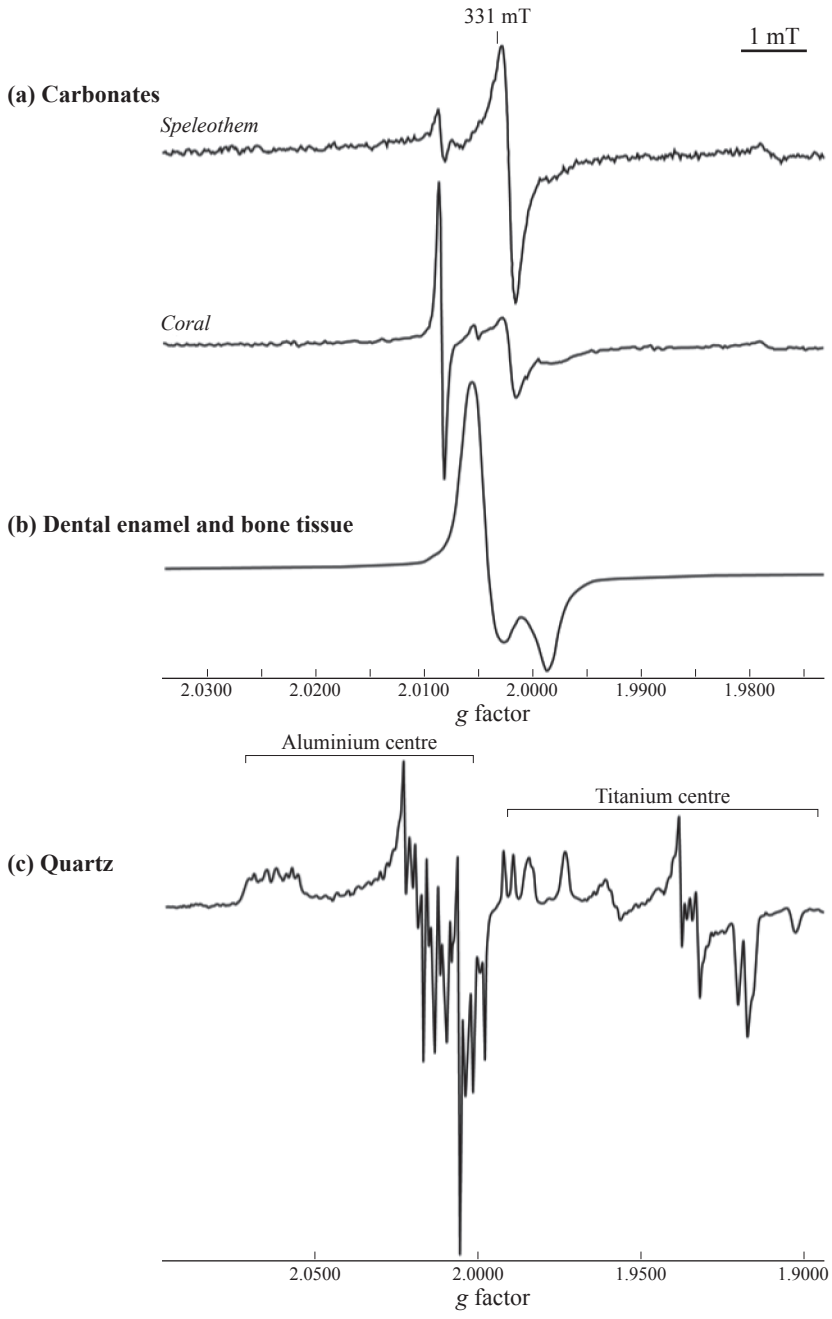

Figure 1.1 - EPR spectra produced by carbonates (cave calcite, corals), dental enamel and quartz in the $g = 2$ region.

(a) Carbonates. Experimental conditions: room temperature, power 5 mW, modulation amplitude 0.1 mT. The carbonate spectra present three radiosensitive lines at $g = 2.0057$; 2.0036; 2.0007 attributed, respectively, to SO_2^-, SO_3^- and CO_2^- radicals associated with a water molecule.

(b) Dental enamel and bone tissue. Experimental conditions: room temperature, power 10 mW, modulation amplitude 0.1 mT. The hydroxyapatite signal used in dating is axial with $g_\perp = 2.0018$; $g_{//} = 1.9977$. It results from the superposition of several signals attributed to carbonated centres (see section 1.3.1).

(c) Quartz. Experimental conditions: $T = 100$ K, power 5 mW, modulation amplitude 0.1 mT. The *aluminium* centre $[AlO_4]^0$ is characterised by $g = 2.0602$; 2.0085; 2.0019 and a hyperfine structure due to the Al nucleus ($I = 5/2$). The *titanium* $[TiO_4]^0$ centres are associated with a compensatory cation (Li^+, Na^+, H^+) and their spectra present a superhyperfine structure due to the cation's nuclear spin ($3/2$ for Li^+ and Na^+, $1/2$ for H^+).

EPR dating can be applied to a wide variety of samples over long time periods. In particular, it can be used to determine chronological reference points for the Lower Pleistocene and the start of the Middle Pleistocene, a period between around 2.0 and 0.5 Ma (figure 1.2).

This method is therefore of great importance, in particular to date samples from the limestone regions of western Europe. For more recent periods, it can be applied in combination with the uranium series (U-Th) method on the same support (dental enamel, mollusc shell, etc.) and the results compared to those obtained by other methods, such as luminescence (thermoluminescence, optically stimulated luminescence) and carbon 14 dating. For recent epochs, the field of application is limited by the radio-sensitivity of the samples.

For more ancient epochs, the number of paramagnetic defects available and their lifetime – if it is too short – are limiting factors which vary depending on the type of sample. Ages of around a million years have been determined from dental enamel and quartz, whereas marine carbonates only appear to be compatible with dating to around a few hundred thousand years.

A summary of the data relating to EPR dating can be found in [Falguères and Bahain, 2002; Grün, 2006]. Application of this method to dating of minerals contained in soils is described in chapter 5 of this volume.

2.5.2 - EPR signatures can be used to monitor the transfer of NOM of various origins to hydrographic networks

Analysis of the spectra in figure 2.4 demonstrates the capacity of EPR tracing to monitor the transfer of NOM from soils to the hydrographic network down to the spillway for the Mercube drainage basin. Figure 2.4a shows spectra for type A horizons for the soils from agricultural and forest sub-basins, and figure 2.4b shows those for the dry residues from water collected in these two sub-basins and at the level of the spillway into lake Geneva.

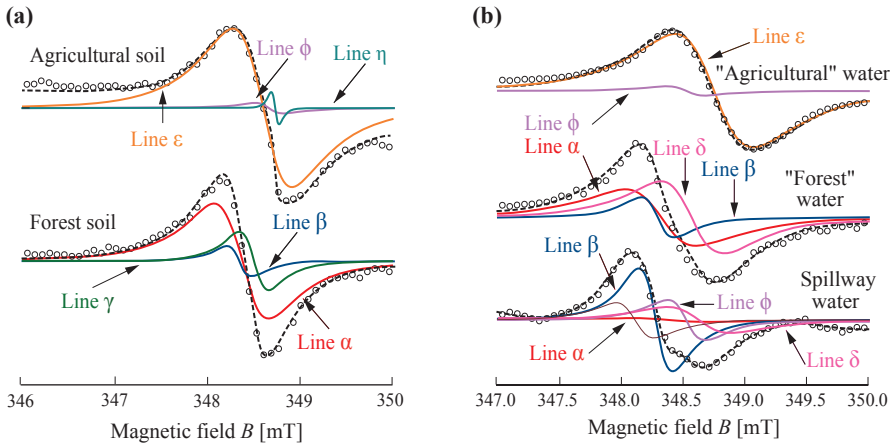

Figure 2.4 - EPR spectra recorded in the $g \sim 2$ region characteristic of NOM. **(a)** Ap horizon for agricultural soil and A horizon for forest soil, **(b)** dry residue from water sampled in the agricultural and forest sub-basins and at the level of the spillway into lake Geneva. The experimental spectra (circles), their simulation (black dashes) and their various components are represented. The parameters used in the simulation and associated barcodes are indicated in table 2.1. Given the value of their *g* factor, some signals which appear during the simulation cannot be attributed to NOM. They are therefore not listed.

Comparison of these spectra leads to the following conclusions:

- ▹ Spectra for water samples collected in the forest and agricultural sub-basins include some of the lines detected in the corresponding soils: lines ε and ϕ characteristic of the agricultural soil are found in "agricultural" waters and lines α and β characteristic of the forest soil are detected in that for "forest" waters. All four lines are also found in water from the spillway into lake Geneva.
- ▹ Line γ characteristic of the forest soil is absent from "forest" water: it is said not to be *water available*.

By providing elements of response to these questions, we hope to guide those who, without being specialists, may have to perform a spin trapping experiment, and more generally help everyone to better understand this method and how it is used in the literature.

3.2 - Implementing the experiment

3.2.1 - Trap selection

The traps most commonly used are either nitroso compounds or aldonitrones, and the addition of a radical $R^{\bullet}$ to these molecules leads to the formation of an aminoxyl, or nitroxide [1] radical, for which the spectrum can be recorded (figure 3.2).

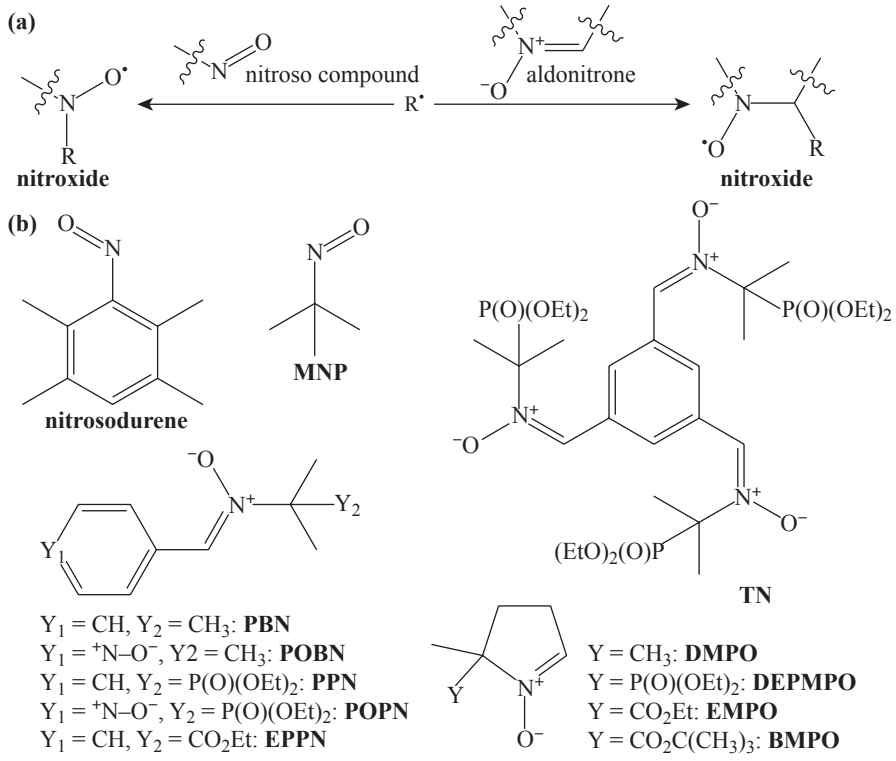

Figure 3.2 - (a) Trapping of a radical $R^{\bullet}$ by a nitroso compound and a nitrone to produce a nitroxyde observable by EPR, **(b)** main traps used.

[1] Although the term "nitroxide" is incorrect to designate an aminoxyl radical, its use is so widespread that in the bibliography from November 2012, we found more than 17,500 references relating to the term "nitroxyde" compared to around 330 for "aminoxyl radical". To avoid any confusion, we will conform in this chapter to the common usage by designating an aminoxyl radical by "nitroxide".

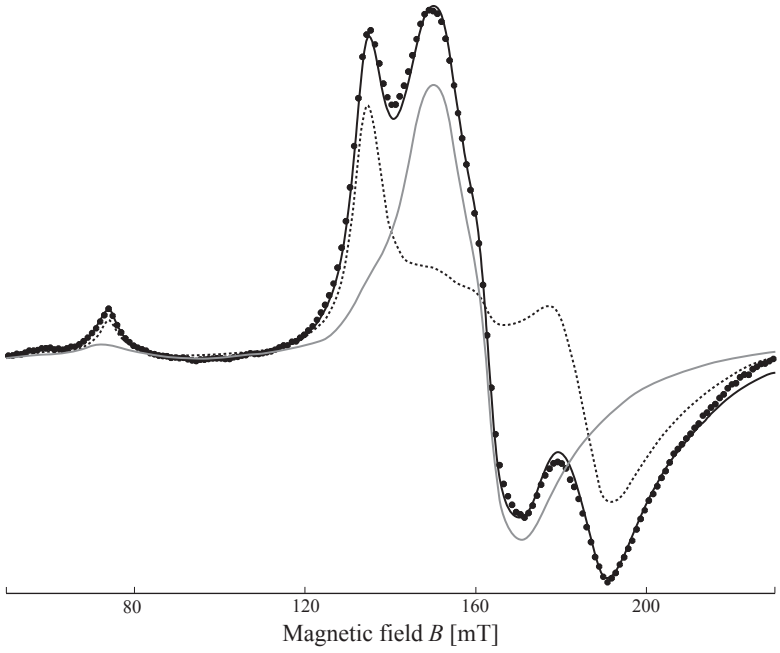

Figure 5.8 - EPR spectrum for the sample collected at 910 cm depth (black dots) and its simulation (continuous black line) obtained by linear combination of the A1 (black dashes) and B4 (continuous grey line) components.

The spectra for samples collected on the profile show that they contain a mixture of two types of kaolinites, an ordered one from sedimentary levels, and a disordered one typical of soil. Their relative proportions, deduced from simulations of the EPR spectra, are in very good agreement with those determined by infrared spectroscopy (figure 5.9).

The persistence of ordered kaolinite in the upper levels of the profile suggests a relatively slow rate of transformation of the kaolinites by dissolution/recrystallisation, and thus the presence of ancient kaolinite populations within lateritic profiles [Balan *et al.*, 2007].

In addition, the transformation of ordered kaolinite to produce disordered kaolinite appears to occur independently of other mineralogical transformations observed in the same lateritic profile, for example, transformation of iron oxides which was studied by Mössbauer spectroscopy, X-ray diffraction and diffuse reflectance UV-visible spectroscopy [Fritsch *et al.,* 2005]. Haematite (Fe_2O_3) and goethite (FeOOH) observed at the bottom of the profile are progressively replaced by aluminium-substituted goethite ($Fe_{0.67}Al_{0.33}OOH$) towards the top,

improving food quality, bioremediation of soils and waters, polymer synthesis, development of biosensors and fuel cells, etc. [Kunammeni *et al.*, 2008].

6.2.1 - A puzzle for spectroscopists: the structure of T_1 and T_2 copper-containing centres

Analysis of the metal atom content of laccases indicated that each molecule contains four copper atoms, and EPR spectrometry rapidly revealed their organisation in the enzyme. At the end of the 1960s, the EPR spectrum for a frozen solution of oxidised laccases from the mushroom *Polyporus versicolor* was shown to contain *two components* of which the intensity indicated a stoichiometry of one centre per molecule: T_1 characterised by $g_{//} = 2.190$, $g_{\perp} = 2.042$, $|A_{//}| = 270$ MHz, $|A_{\perp}| = 29$ MHz, and T_2, characterised by $g_{//} = 2.262$, $g_{\perp} = 2.036$, $|A_{//}| = 530$ MHz, $|A_{\perp}| = 85$ MHz [Malström *et al.*, 1968]. All laccases produce this type of spectrum in the oxidised state. For example, in figure 6.4 we have represented the spectrum for the laccase from *Thielavia arenaria*, a mushroom from the same evolutionary branch as yeasts (single-celled fungi), morels and truffles.

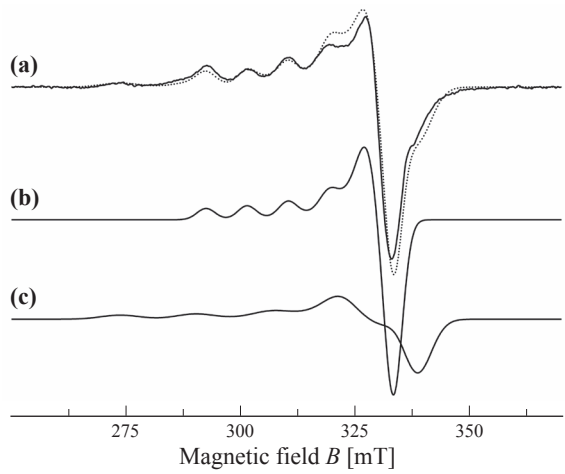

Figure 6.4 - X-band spectrum for a frozen solution of laccase from *Thielavia arenaria.* **(a)** spectrum recorded at 15 K. Microwave: frequency 9.434 GHz, power 1 mW. Modulation: frequency 100 kHz, peak-to-peak amplitude 1 mT. The simulation represented by the dashed line is the sum of the T_1 and T_2 components with the same intensity represented in **(b)** and **(c)**. These simulations were calculated by assuming that the $\tilde{\mathbf{g}}$ and $\tilde{\mathbf{A}}$ matrices had the same principal axes, with Gaussian lines with a full-width-at-half-maximum of σ. T_1: $g_{//} = 2.204$; $g_{\perp} = 2.040$; $A_{//} = 270$ MHz; $A_{\perp} = 30$ MHz; $\sigma_{//} = 140$ MHz; $\sigma_{\perp} = 135$ MHz. T_2: $g_{//} = 2.260$; $g_{\perp} = 2.040$; $A_{//} = 510$ MHz; $A_{\perp} = 105$ MHz; $\sigma_{//} = 300$ MHz; $\sigma_{\perp} = 220$ MHz.

7.3.1 - Line shape: a tool to date terrestrial carbonaceous matter

The EPR spectrum for the CM encased in a rock can therefore readily be determined at room temperature. Like that of the CM in meteorites (figure 7.4), this spectrum contains only *a single unstructured line*. Figure 7.14 shows spectra produced by coals A1 and A3, defined above, and by cherts aged between 45 Ma and 3.5 Ga. The *g* values and peak-to-peak widths ΔB_{pp} for these signals and those produced by other samples of terrestrial CM are listed in table 7.2.

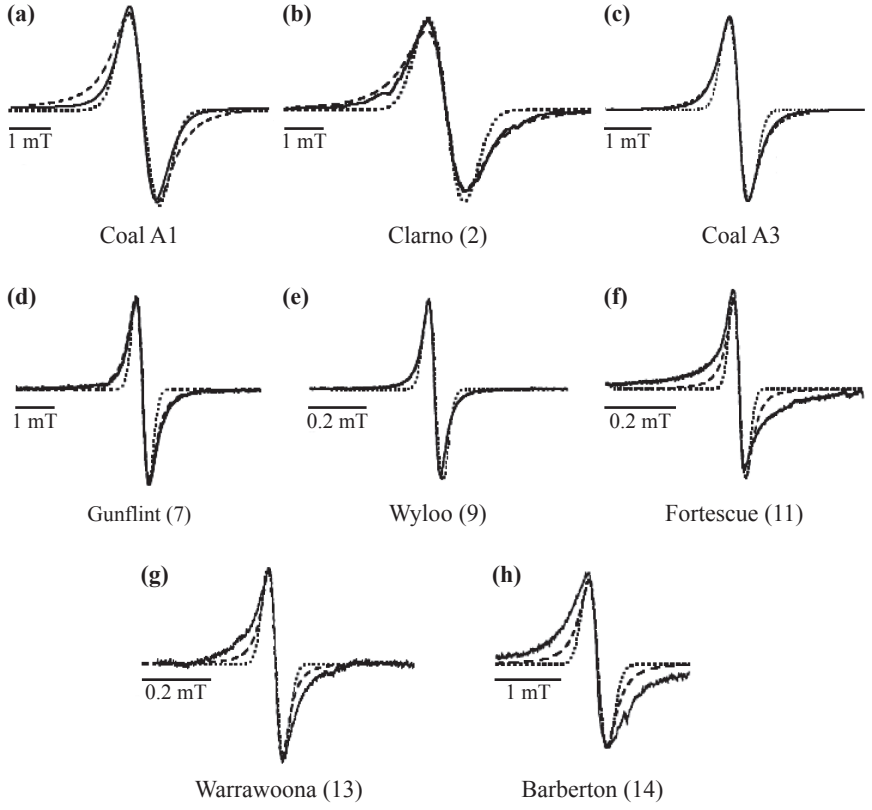

Figure 7.14 - Comparison of EPR spectra for paramagnetic centres in carbonaceous matter from cherts and coal with Gaussian (dotted lines) and Lorentzian (dashed lines) lines. Samples are arranged in increasing order of age and numbered as in table 7.2.

[From Skrzypczak-Bonduelle A. *et al.* (2008) *Appl. Magn. Reson.* **33**: 371-397], *EPR of Radicals in Primitive Organic Matter: A Tool for the Search of Biosignatures of the Most Ancient Traces of Life*, Fig. 3 © 2008 Springer-Verlag, with permission from Springer Science-Business Media]

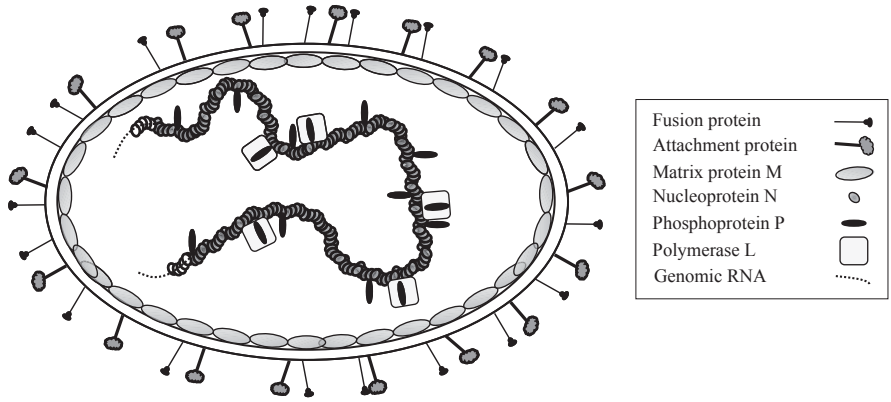

Figure 8.10 - Schematic structure of the measles virus.
Transcription and replication of the virus are ensured by the genomic RNA and the nucleoprotein N/phosphoprotein P complexes.

8.5.1 - Mapping interaction sites for the (N_{TAIL}-XD) complex

To identify the sites on N_{TAIL} interacting with XD, we developed a series of 14 cysteine mutants of N_{TAIL} to successively probe 14 sites using MTSL. Of these 14 sites, 12 are in the 488–525 region which is known to be involved in interaction with XD, and two (positions 407 and 460) are located outside this region (top of figure 8.11). Circular dichroism experiments were used to verify that the cysteine mutations and binding of the label in the series studied affected neither the overall structure of the protein nor its folding [Belle *et al*., 2008]. The EPR spectra for the labelled N_{TAIL} domains were recorded at room temperature, alone and in the presence of XD, and the $h(+1)/h(0)$ ratio was used as an indicator of mobility of the radical (see section 8.3.1). The results are presented in figure 8.11b.

- ▹ As expected, the mobility of the radicals bound to positions 407 and 460 is not affected by the presence of XD.
- ▹ For the labels bound in the 488–502 region, the mobility indicator decreases from 0.85 to around 0.45 in the presence of XD. As an example, we have represented the spectra produced by MTSL bound to position 496 in figure 8.11a.
- ▹ For labels bound in the 505–522 region, the mobility indicator shifts from 0.90 to around 0.80.

9.3 - Study of liquid solutions of diradicals and triradicals: revealing intramolecular exchange

9.3.1 - Diradicals

Several series of compounds can be used to study different aspects of the propagation of the exchange interaction in diradicals.

◇ *Effect of the length of the coupler on exchange interactions*

Up to what distance can exchange interaction between two nitroxide radicals be observed through the phenyl ethynyl moiety (figure 9.5)? To answer this question, the series of *linear diradicals* ***n*p-IN** (n = 2, 3, 5) represented on the left in figure 9.7 was synthesised. Only the structure of the **3p-IN** compound could be determined from X-ray diffraction experiments on a single crystal. The distances between radicals considered to be point radicals, as determined by molecular modelling, were as follows: 1.5 nm for **2p-IN**, 2.1 nm for **3p-IN** and 3.6 nm for **5p-IN**. These linear molecules with numerous aromatic nuclei tend to form aggregates [Breitenkamp and Tew, 2004; Chu and Pang, 2003]. It was thus necessary to use low concentrations, and a xylene/CH_2Cl_2 mixture as solvent. The appearance of narrow hyperfine lines and the UV-visible spectra produced confirm the absence of aggregates in these conditions.

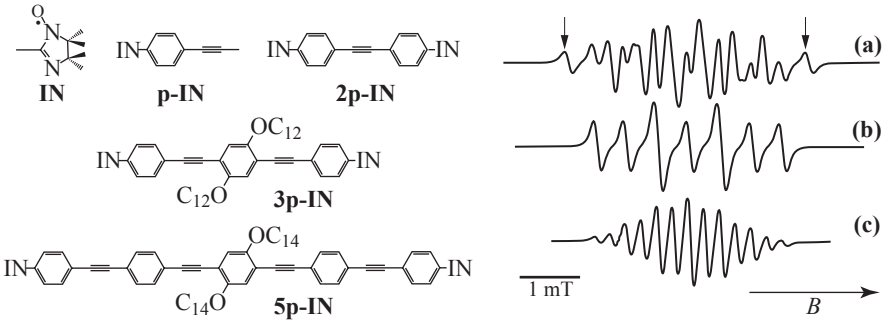

Figure 9.7 - X-band EPR spectra of linear diradicals in a 1:1 xylene/CH_2Cl_2 mixture. **(a) 5p-IN** (6.3×10^{-5} M), **(b) p-IN** (4.3×10^{-5} M), **(c) 3p-IN** (1.1×10^{-5} M). The molecular structures are represented on the left ($OC_{12} = OC_{12}H_{25}$, $OC_{14} = OC_{14}H_{29}$). Spectra **(a)** and **(c)** are centred at the central field of **(b)**, and the slight differences in g_{iso} are taken into account. The spectrum for **2p-IN** is similar to that for **3p-IN (c)**. The arrows indicate lines which are discussed in the text. Microwave **(b)**: frequency 9.775 GHz, power 1 mW. Modulation: frequency 100 kHz, peak-to-peak amplitude 0.06 mT. Same power and modulation for **(a)** and **(c)**. [From Wautelet P. *et al.* (2003) *Journal of Organic Chemistry* **68**: 8025–8036 © 2003 American Chemical Society]

TR-EPR experiments can also be performed with a pulsed spectrometer, by proceeding as indicated in figure 10.6. Pulsed EPR is presented in appendix to this book.

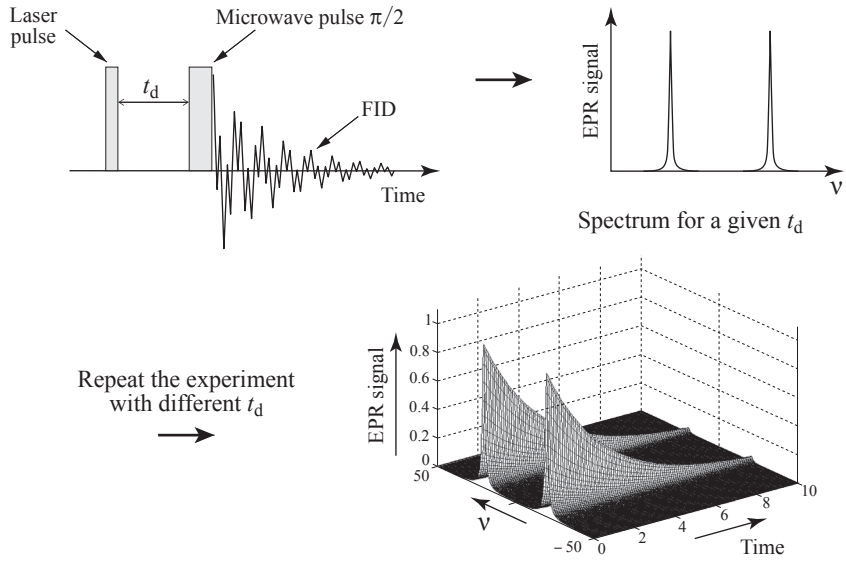

Figure 10.6 - Acquisition of a TR-EPR spectrum with a pulsed spectrometer. For each time value t_d after generation of the paramagnetic species, a series of microwave pulses is applied and the resulting signal is acquired. In the simplest case, a free induction decay (FID) signal is obtained (see appendix 1 to this book), the Fourier transform of which supplies the spectrum as a function of frequency or, as a function of the magnetic field (iso-*t* spectrum) (which is equivalent in this case). [From Maurel V. (2004)]

10.4 - Time-resolved EPR for radicals in solution

10.4.1 - Electron spin polarisation: the CIDEP effect

The spectra obtained by TR-EPR in the first microseconds following the creation of radicals by a photochemical process (typically by nanosecond laser pulses) are very different to those obtained in traditional EPR experiments. Whether recorded by continuous wave or pulsed TR-EPR, these spectra correspond to the *absorption signal* as modulation of the magnetic field or synchronous detection are generally not used at these time scales. The *positions* of the lines are determined by the hyperfine interactions in the radicals studied, but their *intensities* do not follow the usual rules. For example, the spectra can contain alternating *emission* and *absorption* lines (figures 10.7 and 10.8) or simply *emission* lines (figure 10.10). The inhabitual appearance of these spectra is due to the fact that

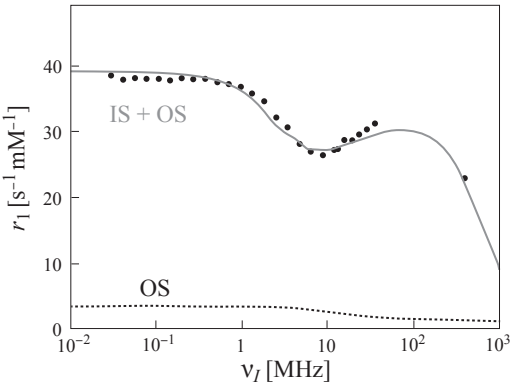

Figure 11.9 - Total relaxivity $r_1(\nu_I)$ (black dots) for water protons in an aqueous solution of Gd(ACX) containing 0.1 M KCl at 298 K. The grey curve is obtained by numerical simulation using the Δ_S, Δ_T, τ_v and g parameters from table 11.2. The value of τ_r was deduced by independent NMR measurements, and the solvation number $q = 4$ was deduced by measuring the lifetime of the luminescence using the method evoked in section 11.5.1. The dashed curve represents the calculated contribution for outer sphere relaxivity. [From Bonnet C.S. *et al.* (2008) *J. Am. Chem. Phys.* **130**: 10401–10413 © 2008 American Chemical Society, reproduced with permission]

Currently, in around 30 % of MRI examinations, radiologists inject Gd^{3+} complexes to improve image contrast and facilitate diagnosis. Figure 11.10 shows the T_1-weighted images of a patient's cerebral tumour before (left) and after (right) injection of the $[Gd(DOTA)(H_2O)]^-$ contrast agent. The contrast agent accelerates the speed of relaxation of the water protons in the tumour which appears as a lighter region, with much better definition, in the right-hand part of the image.

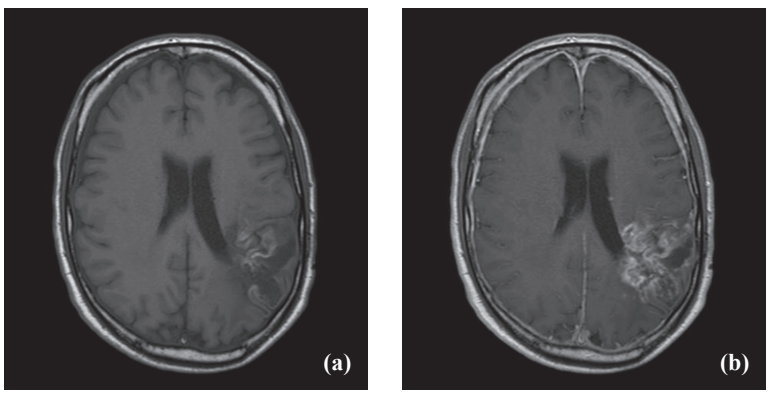

Figure 11.10 - T_1-weighted images acquired at Grenoble University Hospital at 1.5 T, showing a brain tumour **(a)** before and **(b)** after injection of the $[Gd(DOTA)(H_2O)]^-$ contrast agent. The signal for the tumour increases in the presence of the contrast agent – DOTAREM (Guerbet laboratories) – injected at a dose of 0.1 mmol kg^{-1} body weight.